NASA TECHNICAL NOTE

NASA TN D-6580

NASA TN D-6580

DRAG OF A SUPERCRITICAL BODY OF REVOLUTION IN FREE FLIGHT AT TRANSONIC SPEEDS AND COMPARISON WITH WIND-TUNNEL DATA

by J. W. Usry and John W. Wallace

Langley Research Center
Hampton, Va. 23365

NATIONAL AERONAUTICS AND SPACE ADMINISTRATION • WASHINGTON, D. C. • DECEMBER 1971

1. Report No.	2. Government Accession No.	3. Recipient's Catalog No.
NASA TN D-6580		

4. Title and Subtitle	5. Report Date
DRAG OF A SUPERCRITICAL BODY OF REVOLUTION IN FREE FLIGHT AT TRANSONIC SPEEDS AND COMPARISON WITH WIND-TUNNEL DATA	December 1971
	6. Performing Organization Code

7. Author(s)	8. Performing Organization Report No.
J. W. Usry and John W. Wallace	L-8019
	10. Work Unit No.
	742-73-01-01

9. Performing Organization Name and Address	11. Contract or Grant No.
NASA Langley Research Center Hampton, Va. 23365	
	13. Type of Report and Period Covered
12. Sponsoring Agency Name and Address	Technical Note
National Aeronautics and Space Administration Washington, D.C. 20546	14. Sponsoring Agency Code

15. Supplementary Notes

16. Abstract

The forebody drag of a supercritical body of revolution was measured in free flight over a Mach number range of 0.85 to 1.05 and a Reynolds number range of 11.5×10^6 to 19.4×10^6 and was compared with wind-tunnel data. The forebody drag coefficient for a Mach number less than 0.96 was 0.111 compared with the wind-tunnel value of 0.103. A gradual increase in the drag occurred in the Langley 8-foot transonic pressure tunnel at a lower Mach number than in the Langley 16-foot transonic tunnel or in the free-flight test. The sharp drag rise occurred near Mach 0.98 in free flight whereas the rise occurred near Mach 0.99 in the Langley 16-foot transonic tunnel. The sharp rise was not as pronounced in the Langley 8-foot transonic pressure tunnel and was probably affected by tunnel-wall-interference effects. The increase occurred more slowly and at a higher Mach number. These results indicate that the drag measurements made in the wind tunnels near Mach 1 were significantly affected by the relative size of the model and the wind tunnel.

17. Key Words (Suggested by Author(s))	18. Distribution Statement
Transonic drag Supercritical body of revolution Free-flight tests Comparison with wind-tunnel studies	Unclassified – Unlimited

19. Security Classif. (of this report)	20. Security Classif. (of this page)	21. No. of Pages	22. Price*
Unclassified	Unclassified	37	$3.00

*For sale by the National Technical Information Service, Springfield, Virginia 22151

DRAG OF A SUPERCRITICAL BODY OF REVOLUTION IN FREE FLIGHT AT TRANSONIC SPEEDS AND COMPARISON WITH WIND-TUNNEL DATA

By J. W. Usry and John W. Wallace
Langley Research Center

SUMMARY

The forebody drag of a supercritical body of revolution was measured in free flight over a Mach number range of 0.85 to 1.05 and a Reynolds number range of 11.5×10^6 to 19.4×10^6 and was compared with wind-tunnel data. The forebody drag coefficient for a Mach number less than 0.96 was 0.111 compared with the wind-tunnel value of 0.103. A gradual increase in the drag occurred in the Langley 8-foot transonic pressure tunnel at a lower Mach number than in the Langley 16-foot transonic tunnel or in the free-flight test. The sharp drag rise occurred near Mach 0.98 in free flight whereas the rise occurred near Mach 0.99 in the Langley 16-foot transonic tunnel. The sharp rise was not as pronounced in the Langley 8-foot transonic pressure tunnel and was probably affected by tunnel-wall-interference effects. The increase occurred more slowly and at a higher Mach number. These results indicate that the drag measurements made in the wind tunnels near Mach 1 were significantly affected by the relative size of the model and wind tunnel.

INTRODUCTION

A free-flight test was made to provide data at high Reynolds numbers on an aerodynamic configuration designed to fly in the sonic or near-sonic speed regime. The flight test provided sting-free, wall-interference-free data on the transonic drag characteristics of a low-drag body of revolution. These data along with transonic wind-tunnel data measured at the same Mach numbers and Reynolds numbers are being used as part of the data base in applications such as advanced technology aircraft. One approach to the design of these types of aircraft is to define the aerodynamic configuration that allows the aircraft to cruise near sonic speeds without large penalties in performance due to the drag-rise characteristics. This type of design would require a low subsonic drag configuration with a drag divergence Mach number near 1.

Wind-tunnel studies in the Langley 8-foot transonic pressure tunnel (TPT) have produced several bodies of revolution with low drag which appear to have the desired drag divergence characteristics. Acquisition of accurate reliable data near Mach 1 is difficult, however, because of effects due to the tunnel boundaries. For this reason, a free-flight

test of one configuration tested in the Langley 8-foot transonic pressure tunnel and in the Langley 16-foot transonic tunnel (TT) was made for data correlation purposes.

The purpose of this paper is to present the results of the flight test and to compare the data with wind-tunnel results. Specifically, forebody drag and base pressure coefficients are presented and compared with wind-tunnel data over a Mach number range from 0.85 to 1.05 and a Reynolds number range from 11.5×10^6 to 19.4×10^6. A comparison of the drag-rise trends near Mach 1 determined from free-flight and wind-tunnel data is presented and the effects due to test-environment differences are considered. Also histories of the flight-test environment parameters and onboard measurements are presented. The test was conducted at the NASA Wallops Station, Wallops Island, Virginia.

SYMBOLS

a_x accelerometer reading along body X-axis, g units

$C_{A,b}$ base axial drag coefficient, $-C_{p,b}\frac{S_b}{S}$

$C_{A,fb}$ forebody axial-force coefficient, $C_{A,t} - C_{A,b}$

$\Delta C_{A,fb}$ incremental forebody axial-force coefficient, $C_{A,fb} - (C_{A,fb})_{M=0.9}$

$C_{A,t}$ total axial-force coefficient of model, $-\frac{Wa_x}{q_\infty S}$

$C_{D,f}$ skin-friction drag coefficient, based on S

$C_{p,b}$ base pressure coefficient, $\frac{p_b - p_\infty}{q_\infty}$

c chord, centimeters

d_b diameter at base of model, centimeters

d_{max} maximum diameter of model, centimeters

g acceleration due to gravity, m/sec^2

h altitude, meters

h_a airfoil thickness, centimeters

h_r	relative humidity, percent
l	length of model, centimeters
M	Mach number
N_{Re}	Reynolds number, $\frac{\rho_\infty V_\infty l}{\mu_\infty}$
p_b	base pressure, N/m^2
p_s	saturation pressure, N/m^2
p_t	total pressure, N/m^2
p_v	vapor pressure, N/m^2
p_∞	free-stream static pressure, N/m^2
Δp	differential pressure, N/m^2
Δp_α	differential pressure in pitch plane, N/m^2
Δp_β	differential pressure in yaw plane, N/m^2
q_∞	free-stream dynamic pressure, N/m^2
R	gas constant for air
r	body radius, centimeters
S	reference area based on maximum diameter of model, $\pi d_{max}^2/4$, $meters^2$
S_b	reference area based on diameter at base of model, $\pi d_b^2/4$, $meters^2$
T	temperature, K
t	time, seconds
V	earth relative velocity, m/sec

V_s local speed of sound, m/sec

V_w wind velocity, m/sec

V_∞ free-stream velocity, m/sec

W weight of model, 36.35 kgf or 356.47 newtons

X, Y, Z body-axis system

x,y model coordinates, centimeters

x_i any variable listed in table III

α angle of attack, degrees

β angle of sideslip, degrees

η resultant angle, $(\alpha^2 + \beta^2)^{1/2}$, degrees

θ elevation angle, degrees

μ_∞ free-stream viscosity, N-sec/m^2

ρ_∞ free-stream density, kg/m^3

σ standard deviation of variable denoted as subscript

ψ azimuth from true north of payload, degrees

$\psi' = \psi - \psi_w$, degrees

ψ_w azimuth from true north of wind, degrees

RESEARCH MODEL DESCRIPTION

A sketch of the model with dimensions and other details is presented as figure 1 and photographs of the model on the aircraft are shown as figure 2. The aircraft support rig was designed to carry the model so that no protrusions or indentations appeared on the surface of the model. The model was a smooth aerodynamic body of revolution. The

exterior shape was defined to provide low drag characteristics with drag divergence near M = 1. The body radius as a function of longitudinal body station is presented as table I.

The length of the model was 114.30 centimeters and the maximum diameter was 12.70 centimeters. The diameter of the model at the base was 3.28 centimeters. The model was aerodynamically stabilized during the flight by using fins which had a biconvex airfoil section with a thickness-chord ratio of 0.03. The fins were swept 45° and the root chord projected to the body center line was 17.20 centimeters in length. The area rule was used to provide a smooth distribution of the longitudinal cross-sectional area in the vicinity of the fins. Fin dimensions and a set of typical airfoil coordinates are listed in table II. The center of gravity was located 53.46 centimeters aft of the nose tip (46.7 percent of the model length). Differential-pressure ports in the pitch and yaw planes were located on the model as shown in figure 1. A total-pressure port was located at the nose tip and a base-pressure port was located midway between two fins at a distance of 1.32 centimeters from the model center line. A transition strip was located 2.54 centimeters aft of the nose. The strip was 0.127 centimeter wide in the stream direction and consisted of No. 120 carborundum grit particles in a concentration of approximately 20 per centimeter. Transition strip location and grit characteristics were the same as those used on the wind-tunnel model and were determined by using the method of reference 1.

RESEARCH MODEL INSTRUMENTATION

An FM/FM telemeter transmitted six channels of information to ground receiving stations. These transmissions included total pressure, two differential pressure measurements on the nose, two longitudinal accelerations, and base pressure. The following table lists the parameters measured and the range of each instrument used. The expected accuracy (1σ deviation) of each measurement after data reduction to engineering units was assumed to be ± 1 percent of the range of the instrument. An error analysis is presented in the appendix. The orientation of the body-axis system for the results presented in this paper is shown in figure 3.

Measurement	Range of instrument
Total pressure, kN/m^2	0 to 172.4
Differential pressure (two), kN/m^2	0 to 68.9
Longitudinal acceleration, g units	0.25 to -1.00 0.00 to -0.50
Base pressure, kN/m^2	0 to 103.4

TEST ENVIRONMENT

Trajectory Parameters

The test environment was achieved by dropping the research model from an aircraft at an altitude of 9411 meters and a velocity of 182.9 m/sec. The mission profile is shown in figure 4 as a plot of altitude against horizontal range. The time at release from the aircraft was taken as $t = 0$. Time after release and the Mach number range of interest are indicated on the plot. These data were calculated from the best available radar track of the model.

Histories of the altitude, velocity, flight-path angle, Mach number, dynamic pressure, and Reynolds number are shown in figure 5 for the prime data period. Altitude and flight-path angle were calculated from FPQ-6 radar positional data. Free-stream velocity was obtained from FPQ-6 radar positional data, FPQ-6 radar Doppler data, and Jimsphere wind data. Mach number, dynamic pressure, and Reynolds number were calculated from free-stream velocity, atmospheric speed of sound, temperature, and density. Mach number was also calculated by using the tables of reference 2 and the ratio of the total and atmospheric pressure. Accuracies of these parameters and the method used to estimate the accuracy are presented in the appendix.

Atmospheric Parameters

Variations of the atmospheric temperature, pressure, density, speed of sound, and relative humidity with altitude are presented in figure 6. The temperature, pressure, and humidity were measured by use of a standard radiosonde balloon launched at the same time that the model was released from the aircraft. The measurements, therefore, were made within 25 minutes after release. The other parameters were calculated from these measurements. In addition, the parameters from the 1966 U.S. Standard Atmosphere Supplements (ref. 3) are shown for comparison. Accuracies of the measured quantities are based on those in reference 4.

Variations of the atmospheric wind velocity and direction with altitude are shown in figure 7. These data were measured by using the FPS-16 radar-Jimsphere balloon system and have a root-mean-square accuracy of 0.5 m/sec (see ref. 5). The Jimsphere balloon was launched about 25 minutes after the model was released from the aircraft. Therefore, these data were obtained within 50 minutes after model release. These data were used in the calculation of free-stream velocity, Mach number, and dynamic pressure.

RESULTS AND DISCUSSION

Histories of the longitudinal acceleration, total and base pressures, and the differential pressures measured onboard the model are shown in figure 8. The measurements

made by the two longitudinal accelerometers were essentially the same and the curve in figure 8(a) represents both measurements. The primary data period was from $t = 22$ seconds to $t = 36$ seconds corresponding to $M = 0.85$ to 1.05 and Reynolds numbers from 11.5×10^6 to 19.4×10^6.

Angle-of-Attack Effects

A model geometrically similar to the flight model was tested in the Langley 8-foot transonic pressure tunnel and the Langley 16-foot transonic tunnel to determine the variation of the differential pressures with angle of attack and Mach number. These variations were linear with angle of attack for a given Mach number for the range of angles and Mach numbers of interest. The slopes of these curves (differential pressure coefficient per degree) plotted against Mach number are shown in figure 9. The difference in $\partial\left(\Delta p/q_\infty\right)/\partial\alpha$ between the two sets of wind-tunnel data at $M = 1$ is equivalent to a difference in angle of attack of 0.05° for the maximum angles obtained in flight; thus, the faired curve of figure 9 was used with the differential-pressure data of figure 8 measured in flight to estimate the angles of attack and sideslip.

Time histories of the angles of attack, sideslip, and resultant angle are shown in figure 10. These data show that the model flew at a trim angle of attack which decreased with time or increasing Mach number. As the model accelerated through $M = 1$, the trim angle increased to 2° but continued the same decreasing trend after passing through $M = 1.0$. (The estimated standard deviation of the resultant angle at $M = 1$ was 0.4°.) The reason for the model flying at these trim angles is not apparent and cannot be determined from the limited measurements made.

The variation of axial-force coefficient with angle of attack was measured in the wind tunnels at an angle of sideslip of 0° and is shown in figure 11. These data were used to obtain the variation of axial-force coefficient with Mach number at an angle of attack of 0° for comparison with the free-flight test results. In addition, these data are presented to show trends of $C_{A,fb}$ with angle of attack and to illustrate that $C_{A,fb}$ decreases with increasing angle of attack for small angular deviations.

Comparison of Flight Data With Wind-Tunnel Data

The forebody axial-force and base pressure coefficients at the flight trim angles are compared with wind-tunnel data at an angle of attack of 0° in figures 12 and 13. The flight data were calculated as follows:

$$C_{A,fb} = C_{A,t} - (\text{Base axial drag coefficient})$$

$$= -\frac{Wa_x}{q_\infty S} + \left(\frac{p_b - p_\infty}{q_\infty}\right)\frac{S_b}{S}$$

where

$$C_{p,b} = \frac{p_b - p_\infty}{q_\infty}$$

and

$$C_{A,b} = -C_{p,b} \frac{S_b}{S}$$

The 16-foot-tunnel data in figures 12 and 13 were measured at Reynolds numbers from 15.6×10^6 at $M = 0.85$ to 17.04×10^6 at $M = 1.01$ and the 8-foot-tunnel data were measured at a Reynolds number of 16×10^6 for all Mach numbers. The flight Reynolds numbers varied from 11.5×10^6 at $M = 0.85$ to 19.4×10^6 at $M = 1.05$. (See fig. 5.)

The $C_{A,fb}$ from free-flight data (see fig. 12) for $M < 0.96$ was 0.111 whereas the value measured in both wind tunnels was 0.103. The error analysis presented in the appendix shows that one-half of this difference could be attributed to the estimated error in $C_{A,fb}$. The Reynolds number varied during the flight but was essentially constant for both wind-tunnel tests. Also, sting-interference effects could have caused the pressure distribution on the wind-tunnel model afterbody to be considerably different from that on the flight model. Both of these effects could have contributed to the drag level differences for $M < 0.96$.

Figure 13 shows the base pressure coefficient as a function of Mach number with the wind-tunnel data shown for comparison. The base pressures were higher in both tunnels for $M < 0.96$ and indicated that the pressures on the afterbody of the wind-tunnel model could also have been higher. This condition would make the wind-tunnel $C_{A,fb}$ lower than the free-flight values since these pressures were positive. These differences in base pressure alone, however, represent 2.4 percent of the total drag at $M = 0.85$ and become practically insignificant above $M = 0.96$. The sting configurations used in the wind-tunnel tests, however, were designed to minimize sting interference effects by use of the method of reference 6.

Differences which can be attributed to Reynolds number effects are indicated by figure 14 where a theoretical estimate of the skin-friction drag coefficient is shown as a function of Mach number. These coefficients were calculated by using the Sommer-Short T' method and the Karman-Schoenherr flow equation for a turbulent boundary layer and the Blasius-Sutherland equation for a laminar boundary layer. (See refs. 7 and 8.) For this analysis the flow was assumed to be laminar forward of the transition strip and turbulent aft of the strip. Flight conditions were used to obtain the solid curve in figure 14 whereas the broken curve was obtained by using a constant Reynolds number and stagnation

temperature for all Mach numbers and thus simulates the wind-tunnel conditions. Both curves at the top of the figure were calculated by assuming turbulent flow on the body (aft of transition strip) including the fins. The broken curve in the bottom of the figure was obtained by using flight conditions and laminar flow over the fins. These curves indicate that the drag coefficient obtained in flight should be slightly higher than the wind-tunnel values for $M < 0.96$ and slightly less for $M > 0.97$, provided the flow was turbulent over the fins. The actual flow probably was mixed since local Reynolds numbers based on fin chord varied from about 1×10^6 at the fin-body juncture to 0 at the fin tip at the lower Mach numbers and from about 2×10^6 to 0 for the larger Mach numbers. Also, parts of the fins were immersed in the turbulent boundary layer over the body. The model tested in the wind tunnels was geometrically similar and should have had the same flow characteristics as the flight model had, provided the boundary and sting interference effects did not affect the nature of the flow. These data do indicate, however, that considerable differences between the flight and wind-tunnel data could be attributed to Reynolds number and flow character effects.

A comparison of the incremental axial-force coefficients is shown in figure 15 as $\Delta C_{A,fb}$ plotted against Mach number where $\Delta C_{A,fb}$ is the difference in $C_{A,fb}$ from the value at $M = 0.9$. The gradual increase in drag obtained in each of the three tests is probably due to the initial formation of weak shocks on the aft end of the body and the resulting upstream pressure adjustment through the subsonic part of the boundary layer. This gradual increase began at a lower Mach number in the 8-foot transonic pressure tunnel than in either the free-flight test or the 16-foot transonic tunnel and was probably due to boundary interference effects. The $\Delta C_{A,fb}$ data from the free flight and 16-foot transonic tunnel agree very well up to $M = 0.98$. At this point the free-flight drag data increased sharply whereas the sharp rise in the 16-foot-tunnel data occurred near $M = 0.99$. The sharp rise in the data from the 8-foot transonic pressure tunnel was not as pronounced. The increase in drag occurred more slowly and at a higher Mach number. The generally good agreement between the flight data and the 16-foot-tunnel data and the fact that the 16-foot- and 8-foot-tunnel data were obtained under very nearly identical conditions (except for tunnel size) indicate that the drag data obtained near Mach 1 on this model may be significantly affected by factors related to the relative size of the model and the tunnel.

CONCLUDING REMARKS

Drag characteristics of a body of revolution with cruciform fins were determined in free flight over a Mach number range of 0.85 to 1.05 and a Reynolds number range of 11.5×10^6 to 19.4×10^6 and were compared with data measured in the Langley 8-foot

transonic pressure tunnel and the Langley 16-foot transonic tunnel. The free-flight model was dropped from an altitude of 9411 meters at an initial velocity of 182.9 m/sec.

Differences in the flight and wind-tunnel data could be attributed to the combined or individual effects of Reynolds number differences between the flight test and the wind-tunnel tests, flow quality conditions, boundary effects, and instrumentation differences. Further wind-tunnel studies and experimental tests are needed to determine the effects of each of these parameters on the drag.

The axial-force coefficient for a Mach number less than 0.96 was 0.111 in free flight compared with 0.103 for the wind tunnel. A gradual increasing trend in the drag occurred in the Langley 8-foot transonic pressure tunnel at a lower Mach number than in the Langley 16-foot transonic tunnel or in the free-flight test. The sharp drag rise occurred near Mach 0.98 in free-flight data and near Mach 0.99 in the Langley 16-foot transonic tunnel data. The sharp rise was not as pronounced in the data from the Langley 8-foot transonic pressure tunnel. The increase in drag occurred more slowly and at a higher Mach number. These results indicate that the drag measurements made in the wind tunnels near Mach 1 were significantly affected by the relative size of the model and wind tunnel.

Langley Research Center,
National Aeronautics and Space Administration
Hampton, Va., October 27, 1971.

APPENDIX

ERROR ANALYSIS OF FREE-FLIGHT DATA

The root-sum-square (RSS) method for combining errors from independent sources was used to estimate accuracies of the free-flight data. The major parameters of interest are the forebody axial-force coefficient $C_{A,fb}$, Mach number M, and Reynolds number N_{Re}. The assumption was made that the individual error source contributions to the parameters are statistically independent and normally distributed with mean zero. The RSS method may be expressed as follows:

$$\sigma_y = \left[\left(\frac{\partial y}{\partial x_i}\sigma_{x_i}\right)^2 + \ldots + \left(\frac{\partial y}{\partial x_i}\sigma_{x_i}\right)^2 + \ldots + \left(\frac{\partial y}{\partial x_n}\sigma_{x_n}\right)^2\right]^{1/2} \tag{A1}$$

where

σ_y one standard deviation in $y = f(x_i)$

σ_{x_i} one standard deviation in independent variables x_i $(i = 1, 2, 3, \ldots, n)$

$\frac{\partial y}{\partial x_i}$ partial derivative of $y = f(x_i)$ with respect to x_i

The study performed here is concerned with the accuracy of axial-force coefficient, Mach number, and Reynolds number.

The forebody axial-force coefficient is a function of several independent variables and may be expressed as follows:

$$C_{A,fb} = -\frac{2RgT\left[Wa_x - (p_b - p_\infty)S_b\right]}{S\left(p_\infty - 18.147h_r\left\{2.685 + 3.537\times10^{-3}\left[\frac{9}{5}(T - 459.67)\right]^{2.245}\right\}\right)\left[V + V_w(\cos\psi - \psi_w)\cos\theta\right]^2} \tag{A2}$$

By applying the RSS method (eq. (A1)) to equation (A2), the standard deviation of $C_{A,fb}$ can be estimated as follows:

$$\sigma_{C_{A,fb}} = \left[\left(\frac{\partial C_A}{\partial a_x}\sigma_{a_x}\right)^2 + \left(\frac{\partial C_A}{\partial V}\sigma_V\right)^2 + \ldots + \left(\frac{\partial C_A}{\partial p_\infty}\sigma_{p_\infty}\right)^2\right]^{1/2} \tag{A3}$$

Histories of the standard deviations were calculated by using the chain-rule method illustrated in figure 16. Values of the standard deviations used in these calculations are listed in table III. The expected accuracy (1σ deviation) of each onboard measurement after data reduction to engineering units was assumed to be ±1 percent of the range of the instrument.

Standard deviations of the wind data (σ_{V_w} and σ_{ψ_w}) and atmospheric data (σ_T, σ_{h_r}, and σ_{p_∞}) were obtained from references 4 and 5. Standard deviations for radar data (σ_V, σ_ψ, and σ_θ) were obtained from a radar study conducted at Wallops Island, Virginia.

Table IV presents the values and the estimated standard deviations of $C_{A,fb}$, M, and N_{Re} at $M = 1$. The values and estimated standard deviations for the intermediate variables in these estimations are also listed. The standard deviation of $C_{A,fb}$ is about 2 percent of the calculated value at $M = 1.00$. The standard deviation is less than 0.2 percent for M and less than 0.4 percent for N_{Re}.

Figure 17 shows the variation of the error contribution of four of the basic variables and $\sigma_{C_{A,fb}}$ with M. The four variables make the largest error contributions to $\sigma_{C_{A,fb}}$ and the error contribution of the a_x measurement is an order of magnitude larger than the other three error sources and clearly illustrates the need to improve the accuracy of the complete data acquisition system.

Figure 18 shows the variation of $C_{A,fb}$ and $C_{A,fb} \pm \sigma_{C_{A,fb}}$ with M. Also indicated in the figure is $M \pm \sigma_M$ at $M = 0.97$. The error in $C_{A,fb}$ at $M = 0.80$ is 8 percent of $C_{A,fb}$ and decreases with increasing M. At $M = 1$, the error is 2 percent.

REFERENCES

1. Braslow, Albert L.; and Knox, Eugene C.: Simplified Method for Determination of Critical Height of Distributed Roughness Particles for Boundary-Layer Transition at Mach Numbers From 0 to 5. NACA TN 4363, 1958.

2. Anon.: Equations, Tables, and Charts for Compressible Flow. NACA Rep. 1135, 1953.

3. Anon.: U.S. Standard Atmosphere Supplements, 1966. Environ. Sci. Serv. Admin., NASA, and U.S. Air Force.

4. Anon.: Environmental-Measuring Equipment Used by Air Weather Service in Support of Air Force and Army Operations. AWS Pamphlet 105-3, U.S. Air Weather Service, Nov. 10, 1967. (Available from DDC as AD 822 895.)

5. Scoggins, James R.: Sphere Behavior and the Measurement of Wind Profiles. NASA TN D-3994, 1967.

6. Cahn, Maurice S.: An Experimental Investigation of Sting-Support Effects on Drag and a Comparison With Jet Effects at Transonic Speeds. NACA Rep. 1353, 1958. (Supersedes NACA RM L56F18a.)

7. Sommer, Simon C.; and Short, Barbara J.: Free-Flight Measurements of Turbulent-Boundary-Layer Skin Friction in the Presence of Severe Aerodynamic Heating at Mach Numbers From 2.8 to 7.0. NACA TN 3391, 1955.

8. Chapman, Dean R.; and Rubesin, Morris W.: Temperature and Velocity Profiles in the Compressible Laminar Boundary Layer With Arbitrary Distribution of Surface Temperature. J. Aeronaut. Sci., vol. 16, no. 9, Sept. 1949, pp. 547-565.

TABLE I.- COORDINATES OF BODY

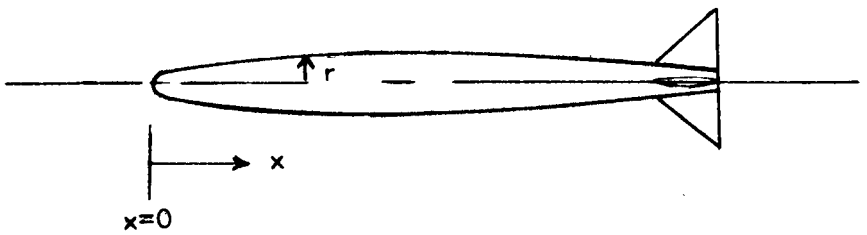

x, cm	r, cm	x, cm	r, cm	x, cm	r, cm
0.0	0.0	22.86	5.30	78.74	6.00
.25	.83	25.40	5.47	81.28	5.91
.51	1.14	27.94	5.62	83.82	5.80
.76	1.37	30.48	5.75	86.36	5.68
1.02	1.55	33.02	5.86	88.90	5.54
1.27	1.71	35.56	5.96	91.44	5.38
1.52	1.85	38.10	6.05	93.98	5.20
1.78	1.98	40.64	6.12	96.52	5.00
2.03	2.10	43.18	6.19	99.06	4.77
2.29	2.20	45.72	6.24	100.33	4.64
2.54	2.30	48.26	6.28	101.60	4.50
3.81	2.73	50.80	6.31	102.87	4.33
5.08	3.07	53.34	6.34	104.14	4.17
6.35	3.35	55.88	6.35	105.41	3.86
7.62	3.60	58.42	6.35	106.68	3.56
8.89	3.82	60.96	6.34	107.95	3.23
10.16	4.02	63.50	6.33	109.22	2.85
11.43	4.20	66.04	6.30	110.49	2.47
12.70	4.36	68.58	6.26	111.76	2.09
15.24	4.65	71.12	6.21	113.03	1.77
17.78	4.90	73.66	6.16	113.66	1.67
20.32	5.11	76.20	6.09	114.30	1.64

TABLE II.- FIN DIMENSIONS

[The coordinates of any airfoil section in the chordwise direction are given by

$$y = 2\left(\frac{h_a}{c}\right)\frac{x}{c}\left(1 - \frac{x}{c}\right)c$$

where $\frac{h_a}{c} = 0.03$.]

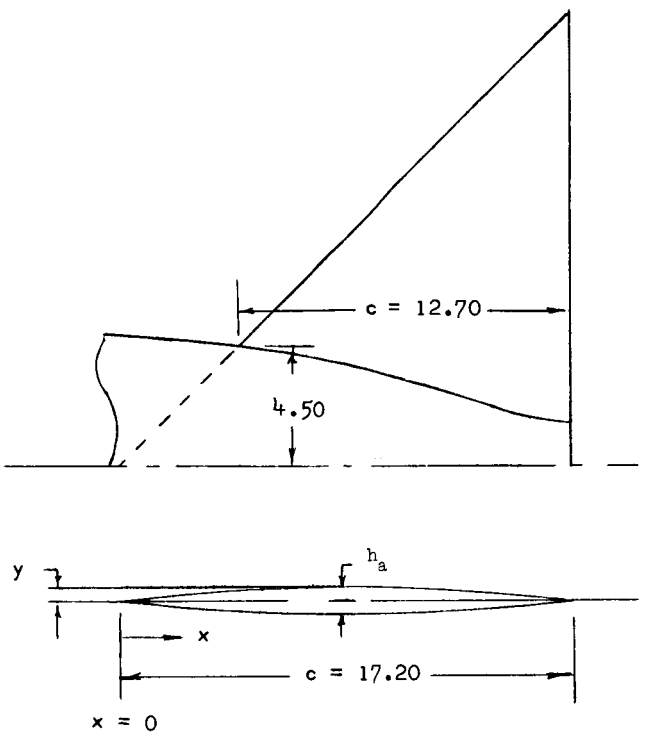

Typical coordinates of airfoil section, c = 12.70 cm

x, cm	y, cm	x, cm	y, cm	x, cm	y, cm	x, cm	y, cm
0.0000	0.0000	3.3020	0.1466	6.6040	0.1902	9.9060	0.1308
.2540	.0149	3.5560	.1537	6.8580	.1892	10.1600	.1219
.5080	.0292	3.8100	.1600	7.1120	.1877	10.4140	.1125
.7620	.0429	4.0640	.1659	7.3660	.1857	10.6680	.1024
1.0160	.0561	4.3180	.1709	7.6200	.1829	10.9220	.0917
1.2700	.0686	4.5720	.1755	7.8740	.1796	11.1760	.0805
1.5240	.0805	4.8260	.1796	8.1280	.1755	11.4300	.0686
1.7780	.0917	5.0800	.1829	8.3820	.1709	11.6840	.0561
2.0320	.1024	5.3340	.1857	8.6360	.1659	11.9380	.0429
2.2860	.1125	5.5880	.1877	8.8900	.1600	12.1920	.0292
2.5400	.1219	5.8420	.1892	9.1440	.1537	12.4460	.0149
2.7940	.1308	6.0960	.1902	9.3980	.1466	12.7000	.0000
3.0480	.1389	6.3500	.1905	9.6520	.1389		

TABLE III.- ASSUMED VALUES OF STANDARD DEVIATIONS (1σ) FOR CALCULATIONS

σ_{a_x}, g	0.005
σ_{p_b}, kN/m^2	1.034
σ_{p_t}, kN/m^2	1.724
σ_{V_w}, m/sec	0.5000
σ_{ψ_w}, rad	0.01745
σ_V, m/sec	0.3048
σ_ψ, rad	0.00015
σ_θ, rad	0.00015
σ_T, K	0.70
σ_{h_r} for –	
273.15 K > T ≧ 233.15 K	0.033
T ≦ 273.15 K	0.017
σ_{p_∞} for –	
h < 3048 m	0.023
3048 m < h < 6096 m	0.033
6096 m < h < 9144 m	0.040

TABLE IV.- CALCULATED STANDARD DEVIATIONS FOR M = 1

Parameter	Value	Standard deviation
$C_{A,fb}$	0.191	0.004
M	1.000	0.002
N_{Re}	16.29×10^6	0.06×10^6
p_s, kN/m^2	0.21	0.01
p_v, kN/m^2	0.06	0.01
ψ', rad	0.33	0.02
ρ_∞, kg/m^3	0.729	0.002
V_∞, m/s	325.2	0.4
q_∞, kN/m^2	38.6	0.1
$C_{A,t}$	0.181	0.004
$C_{A,b}$	0.011	0.002
V_s, m/s	325.2	0.4
μ_∞, N-sec/m^2	1.664×10^{-8}	0.004×10^{-8}

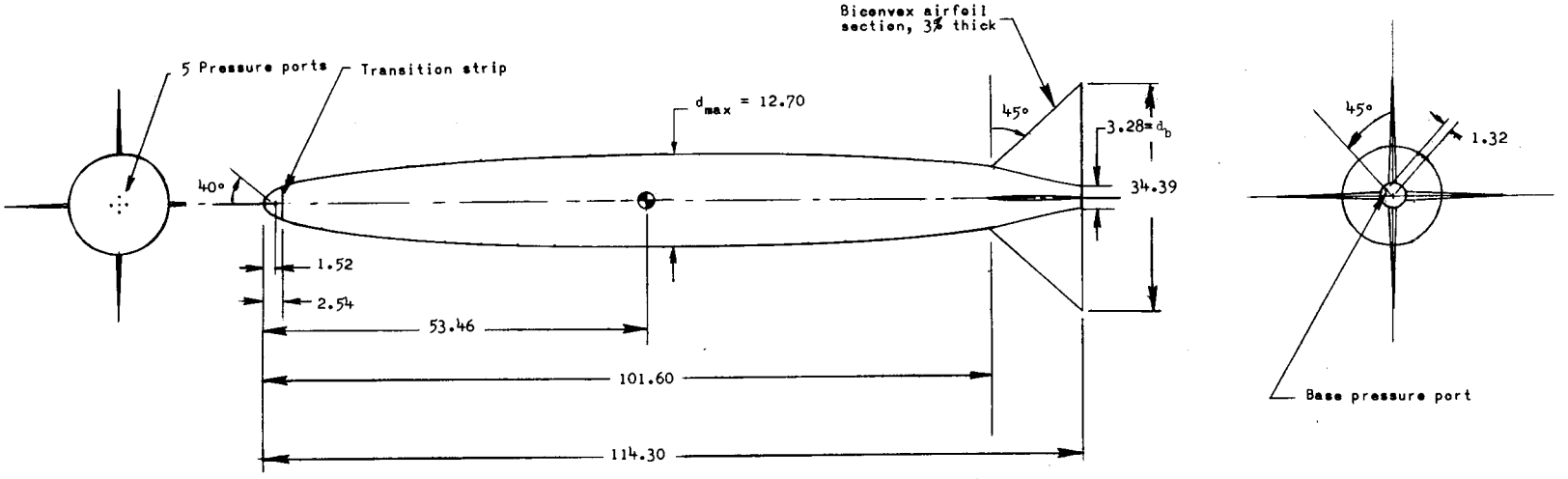

Figure 1.- Sketch of research model. Dimensions are in centimeters.

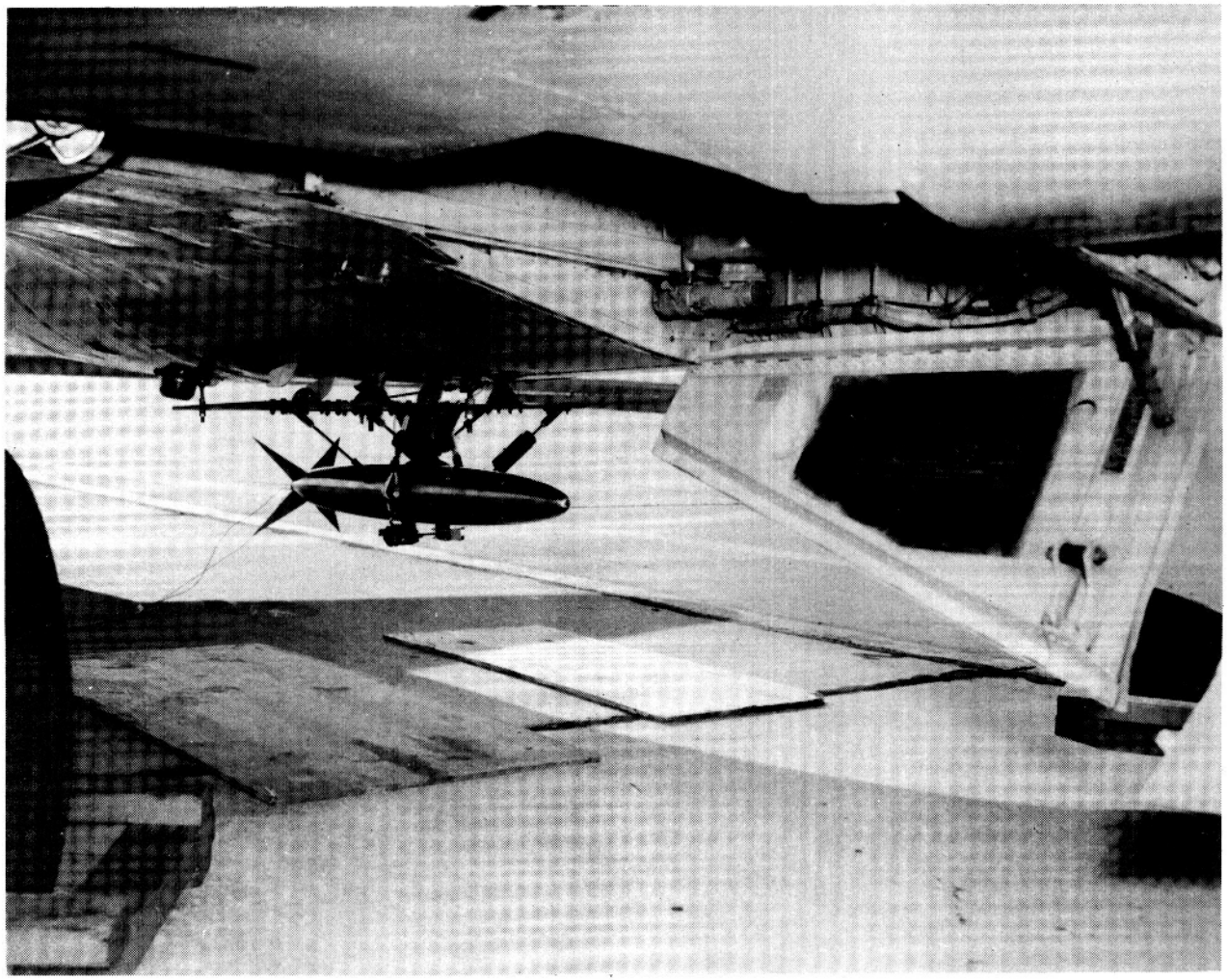

L-70-140

(a) Front quarter view.

Figure 2.- Photographs of model on aircraft.

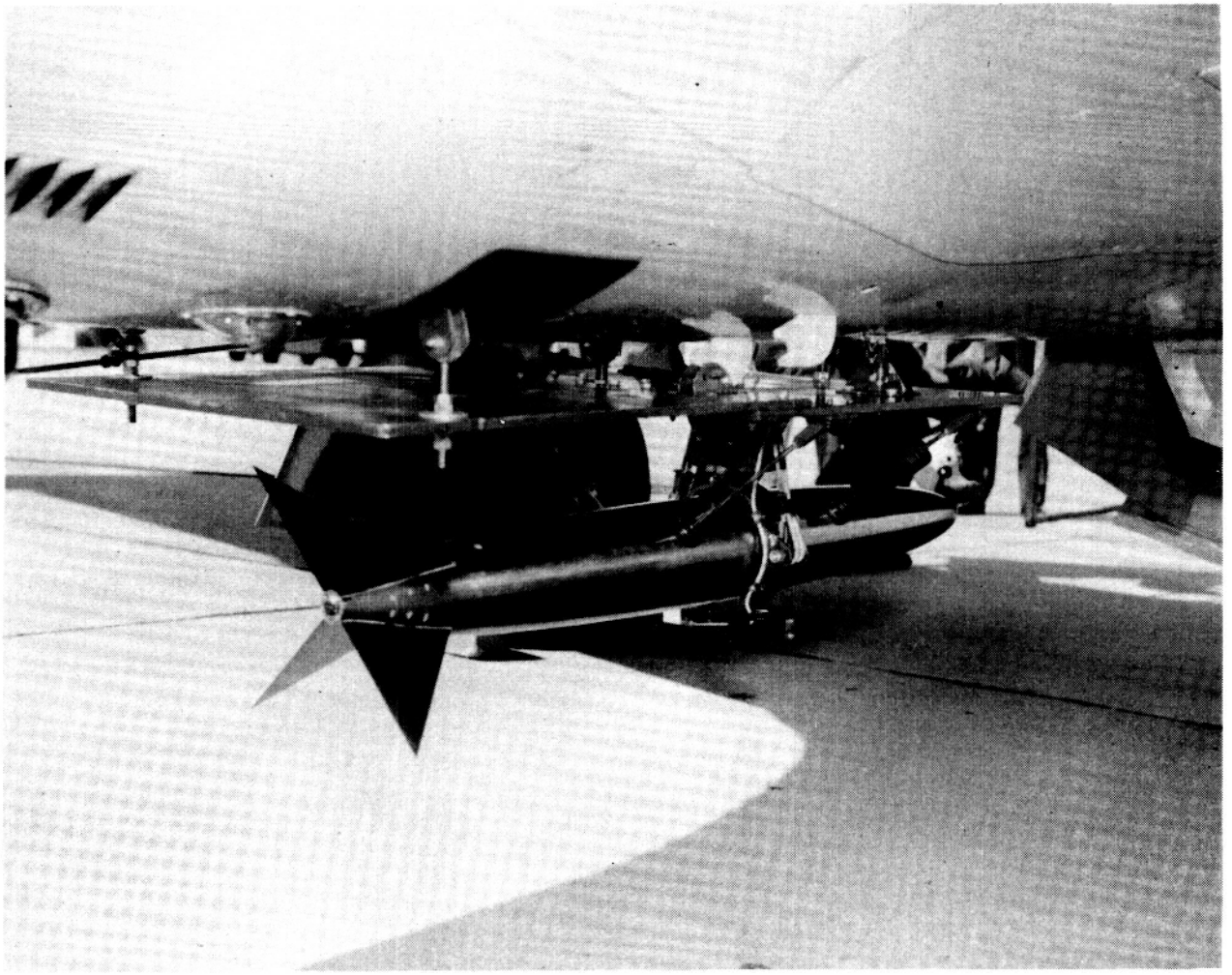

L-70-7372

(b) Rear quarter view.

Figure 2.- Concluded.

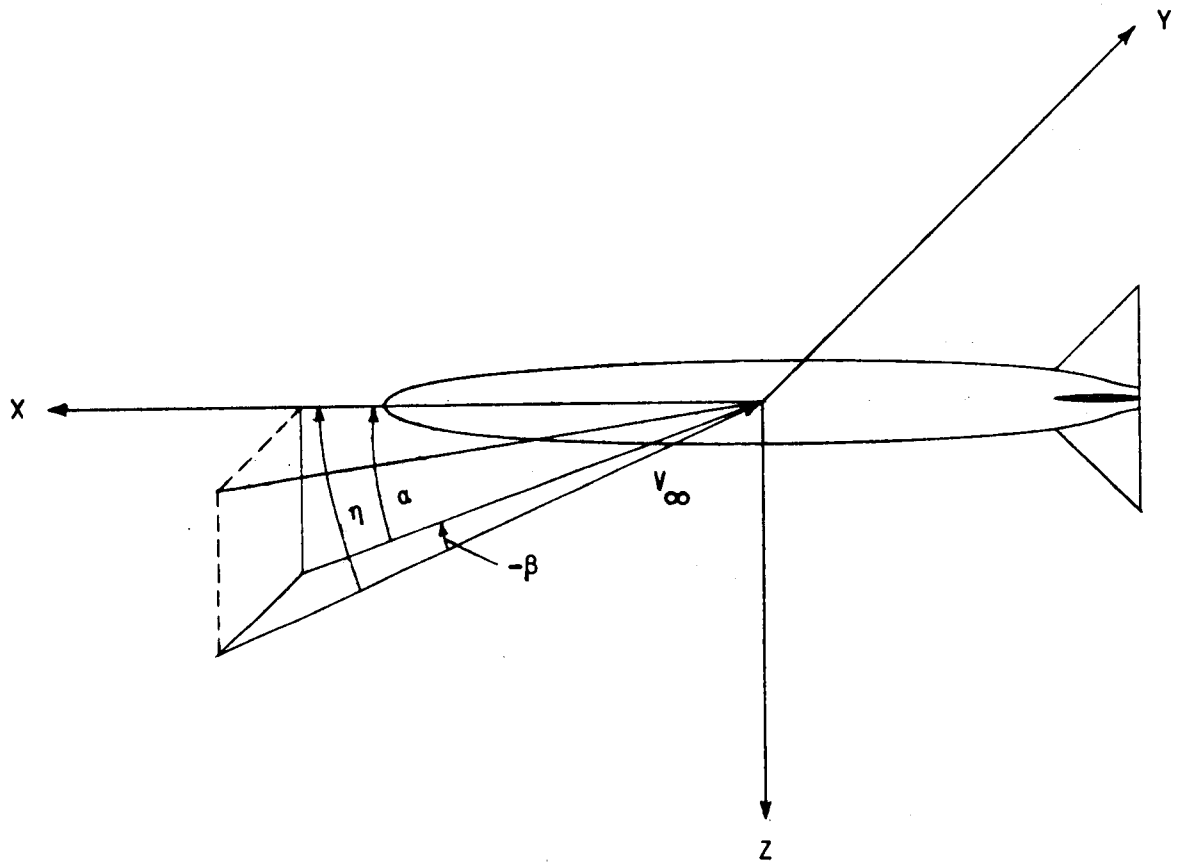

Figure 3.- Body-axis-system orientation.

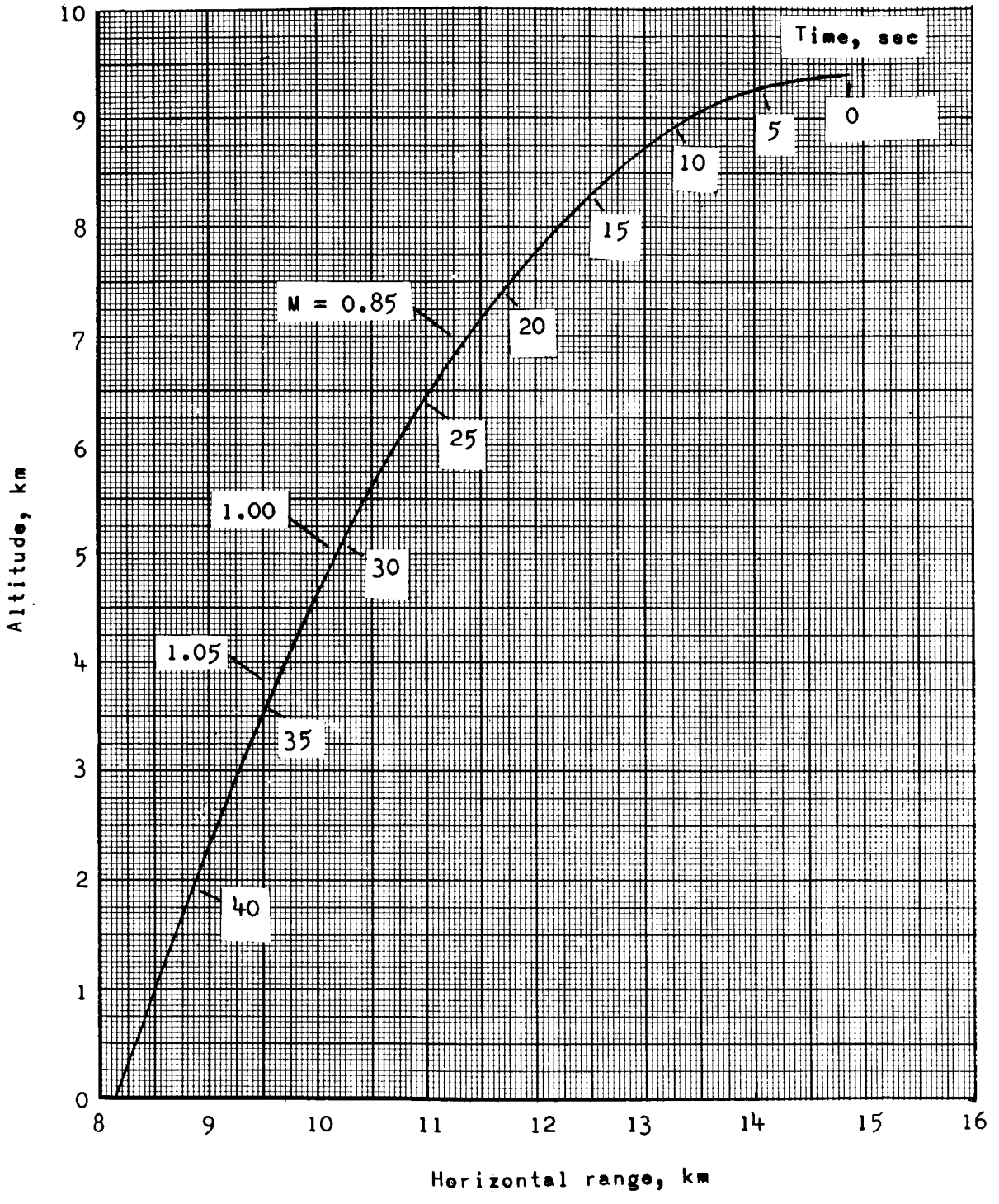

Figure 4.- Variation of altitude with horizontal range based on radar data.

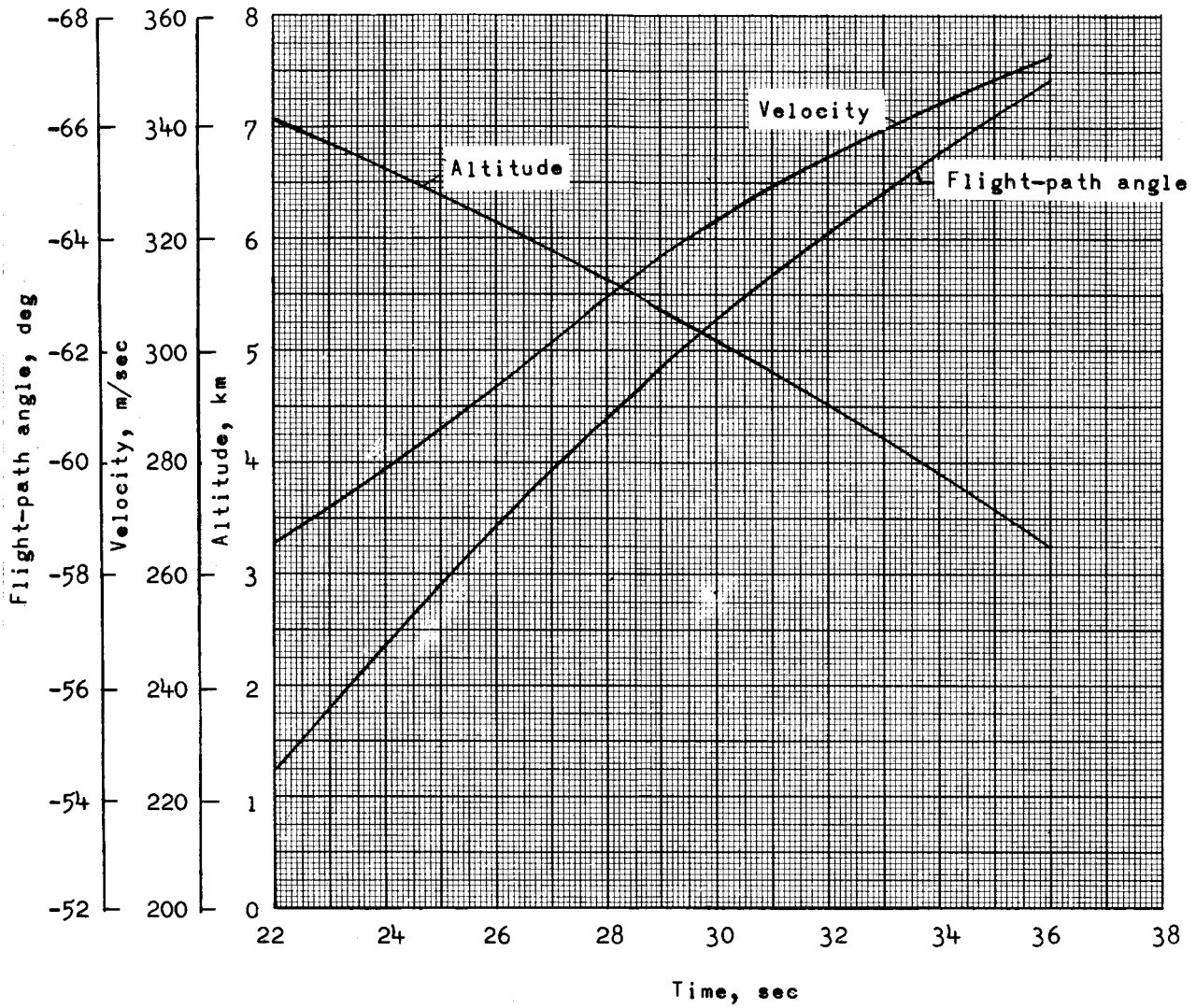

(a) Time histories of altitude, velocity, and flight-path angle.

Figure 5.- Time histories of test conditions.

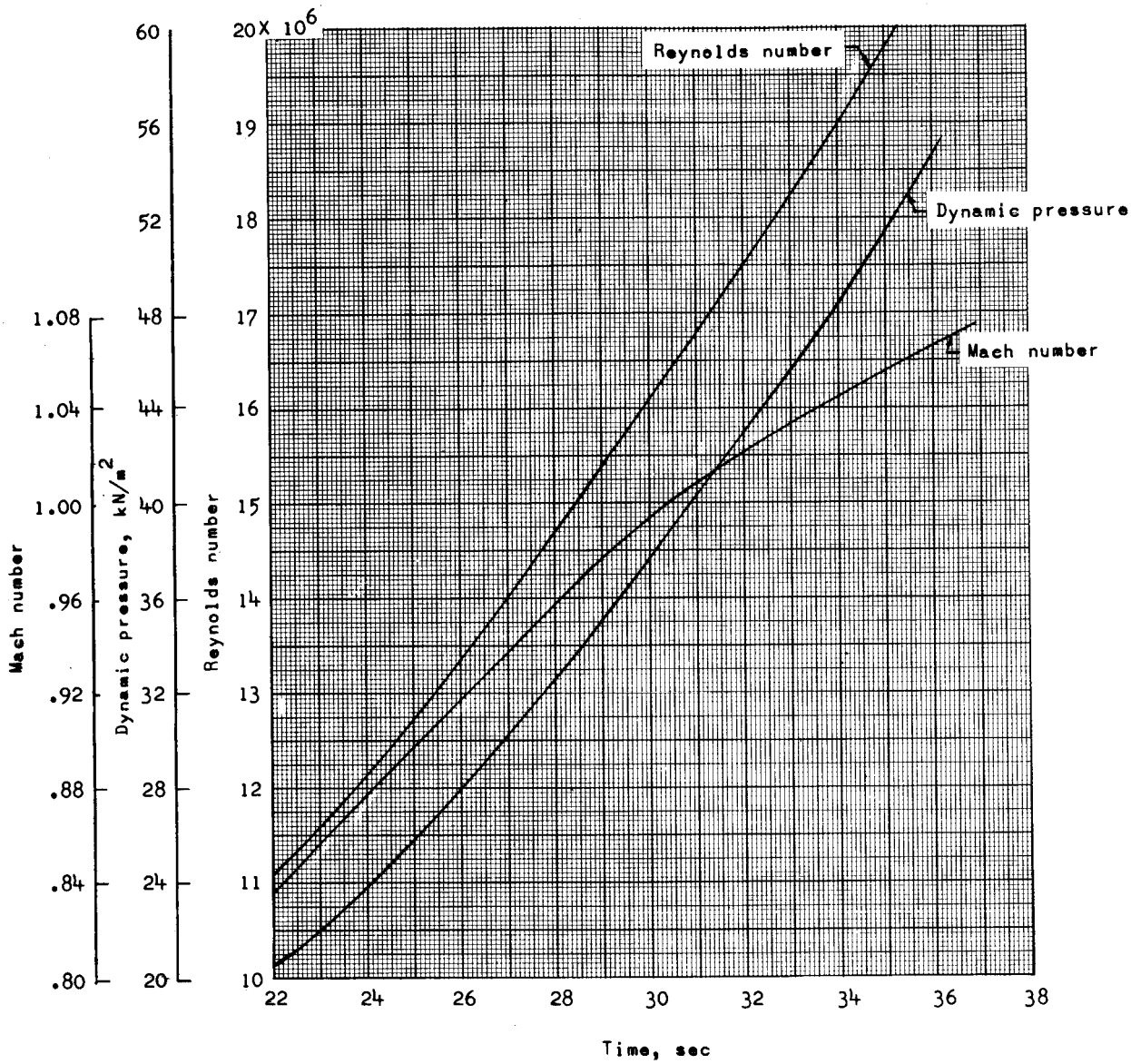

(b) Time histories of Mach number, dynamic pressure, and Reynolds number.

Figure 5.- Concluded.

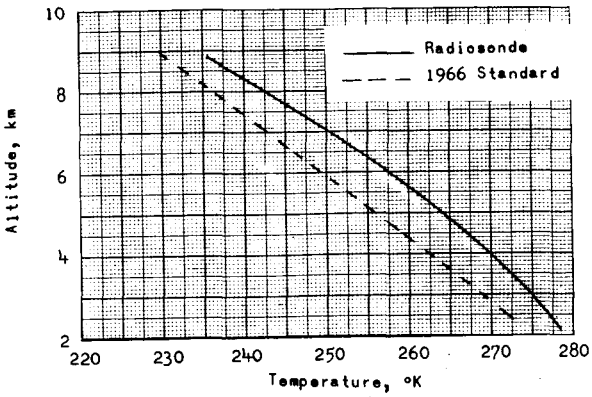

(a) Temperature.

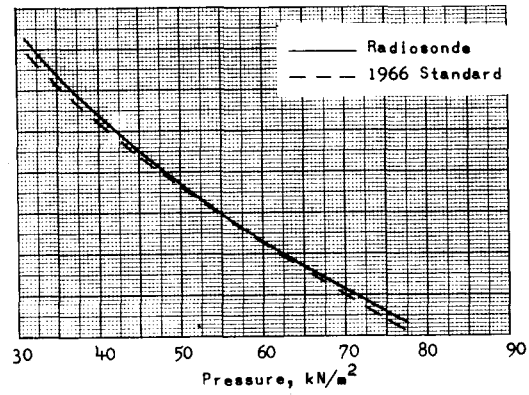

(b) Pressure.

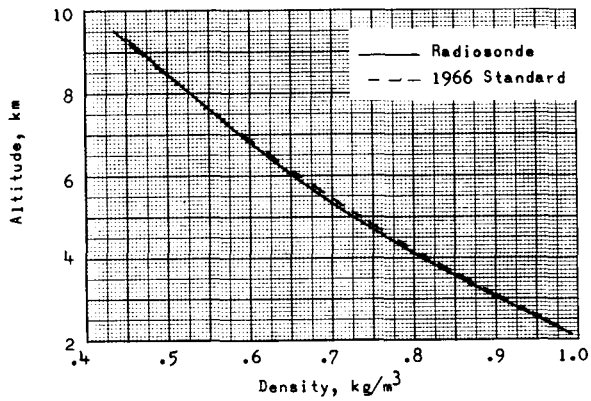

(c) Density.

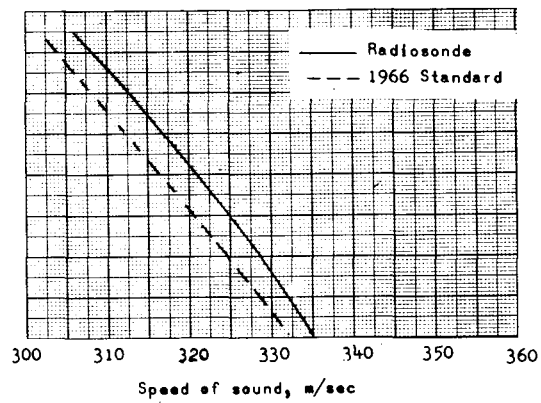

(d) Speed of sound.

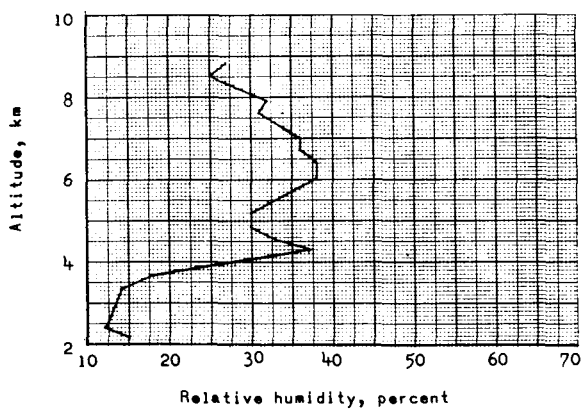

(e) Relative humidity.

Figure 6.- Atmospheric properties as a function of altitude.

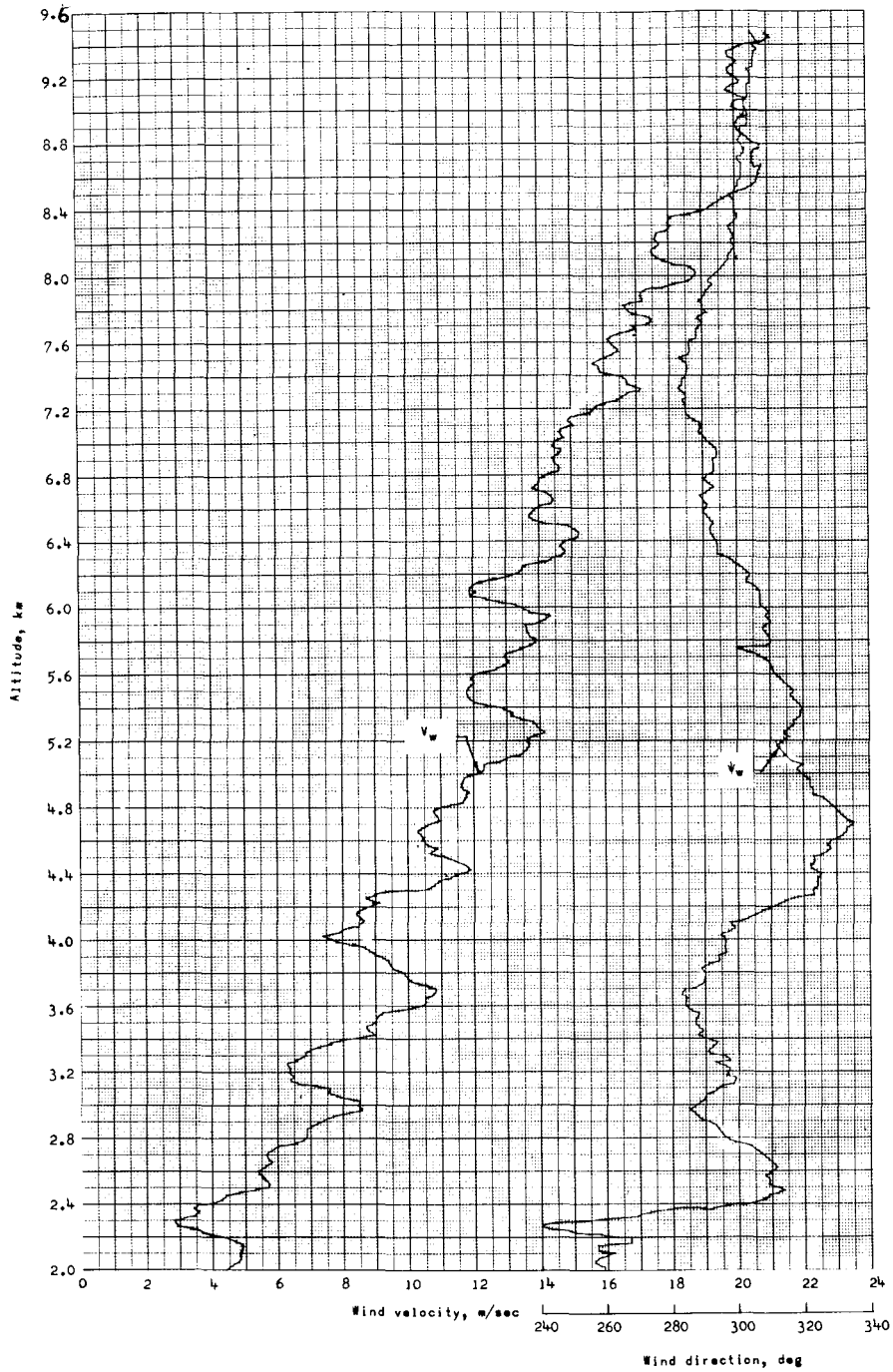

Figure 7.- Variation of wind velocity and direction with altitude.

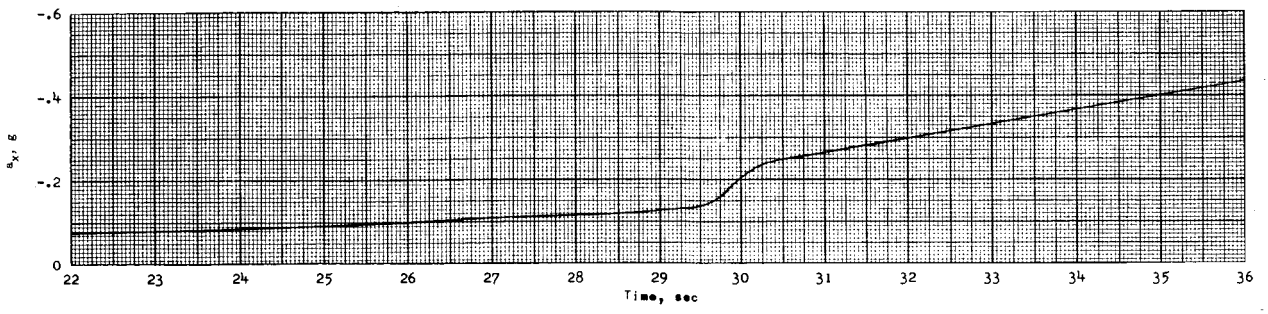

(a) Longitudinal acceleration.

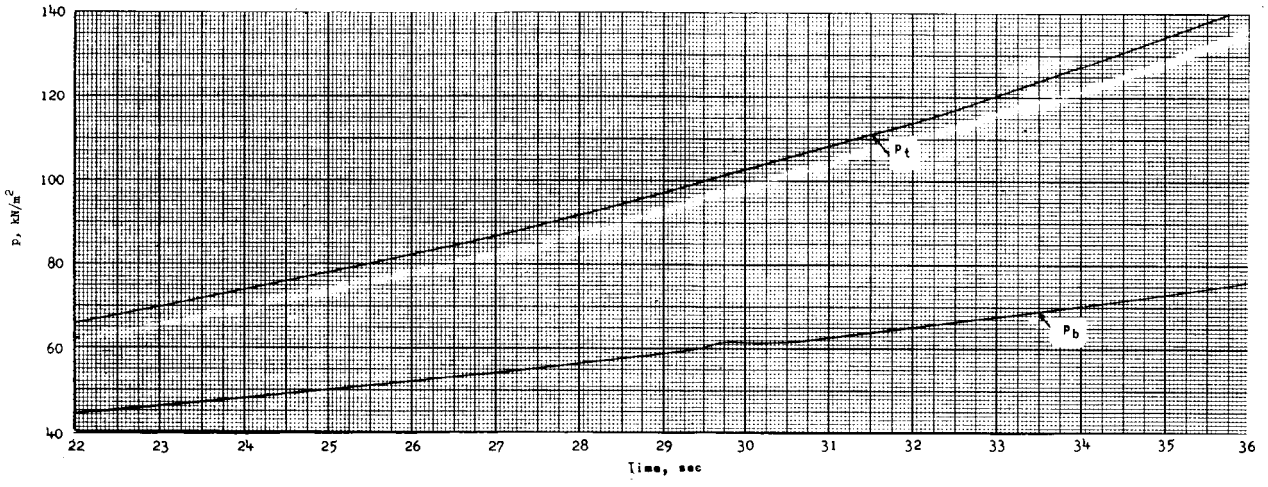

(b) Total and base pressures.

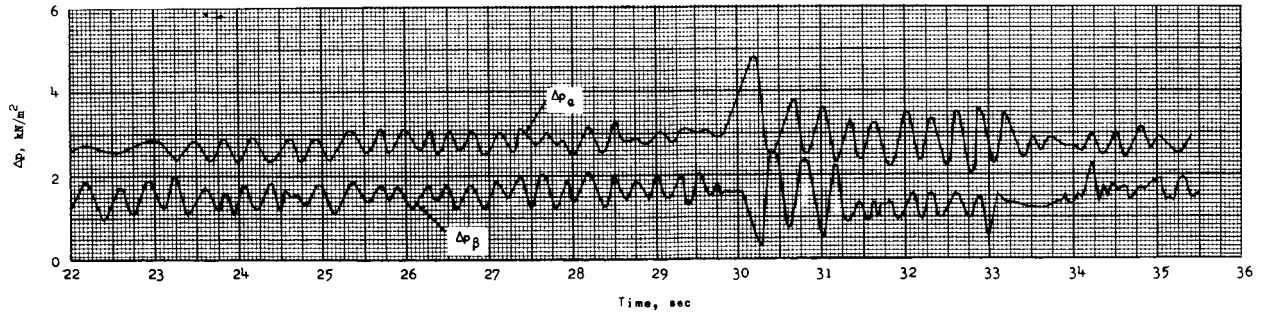

(c) Differential pressures in pitch and yaw planes.

Figure 8.- Time histories of data from onboard instruments.

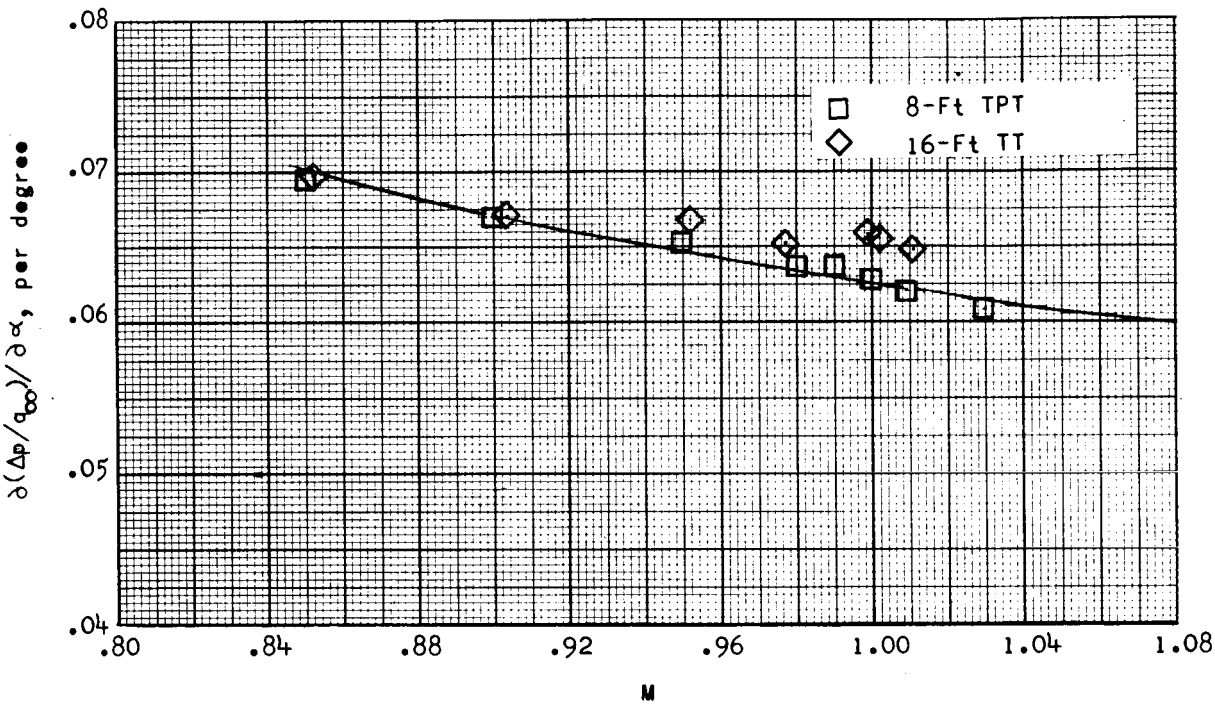

Figure 9.- Variation of differential pressure coefficient per degree angular displacement with Mach number.

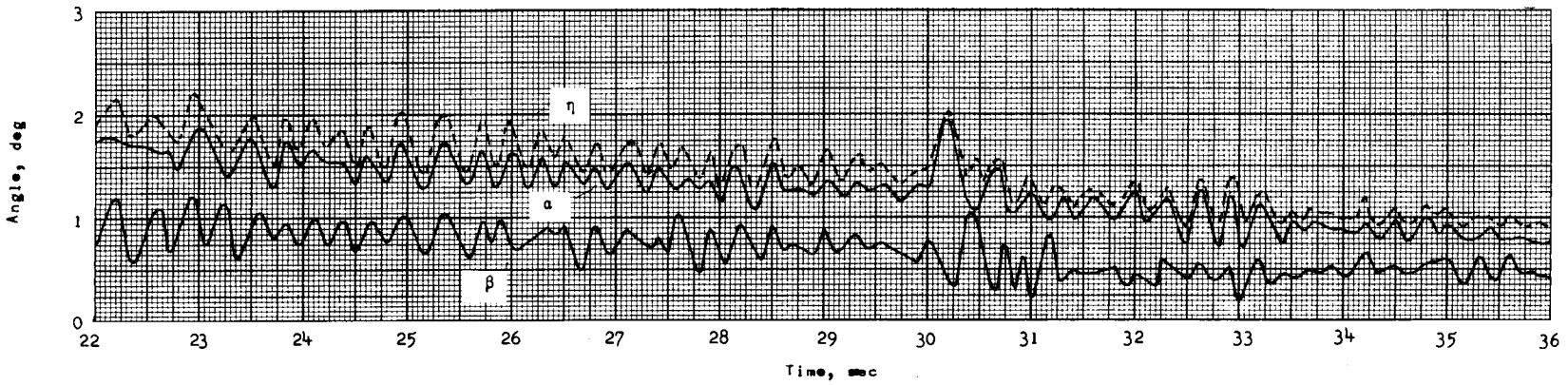

Figure 10.- Time histories of angles of attack, sideslip, and resultant angle.

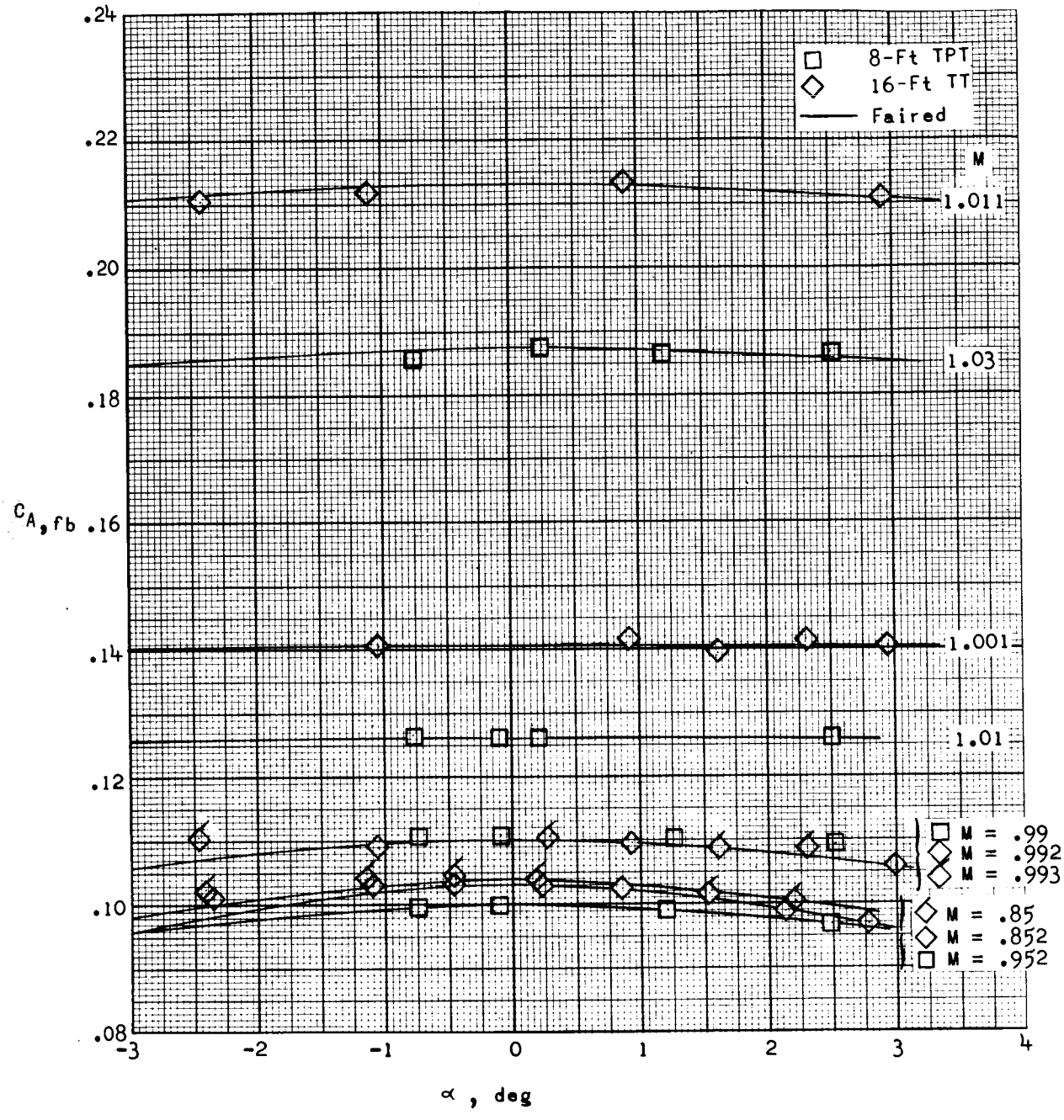

Figure 11.- Variation of forebody axial-force coefficient with angle of attack from the Langley 8-foot transonic pressure tunnel and the Langley 16-foot transonic tunnel.

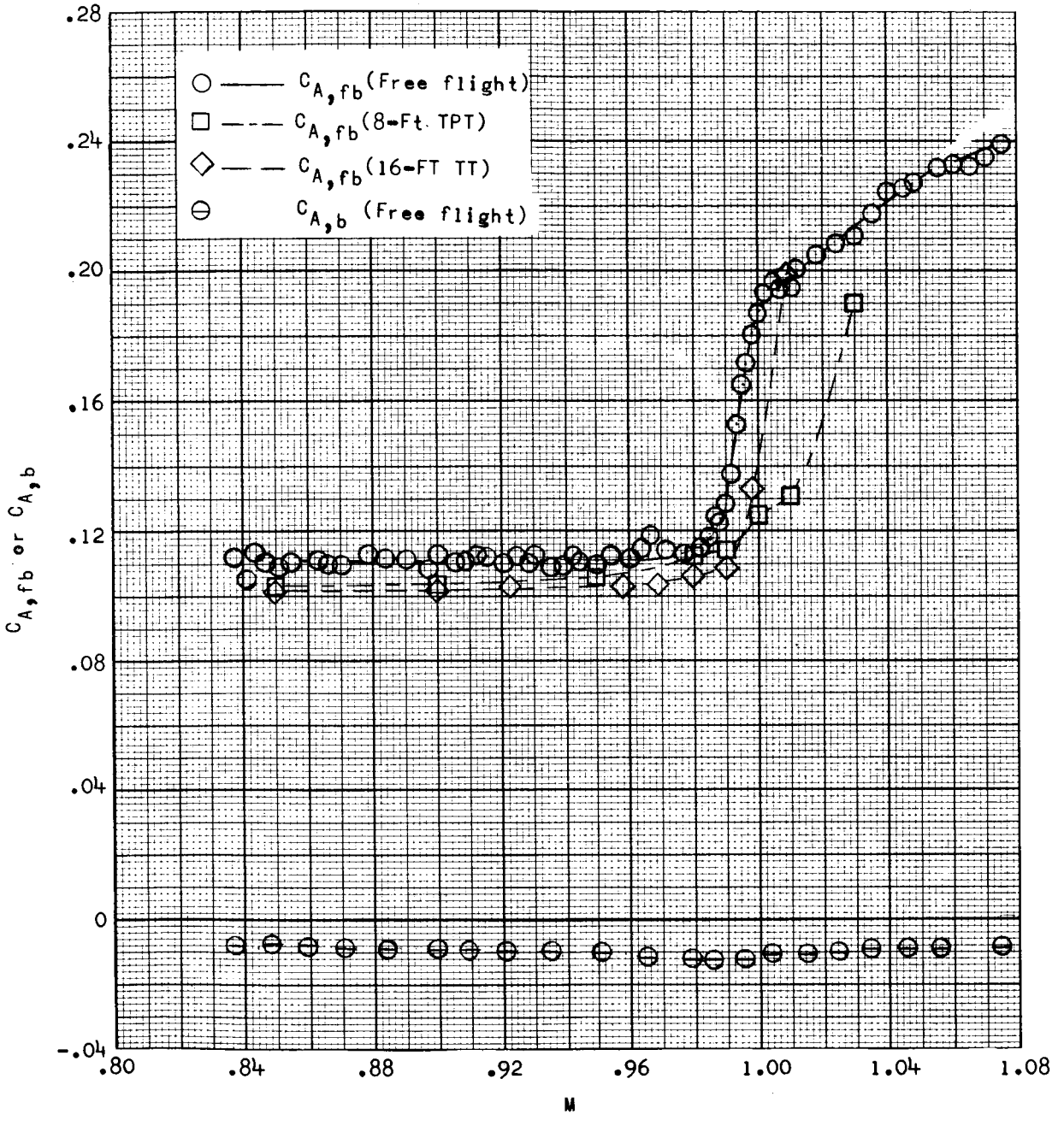

Figure 12.- Variation of forebody axial-force and base drag coefficients with Mach number.

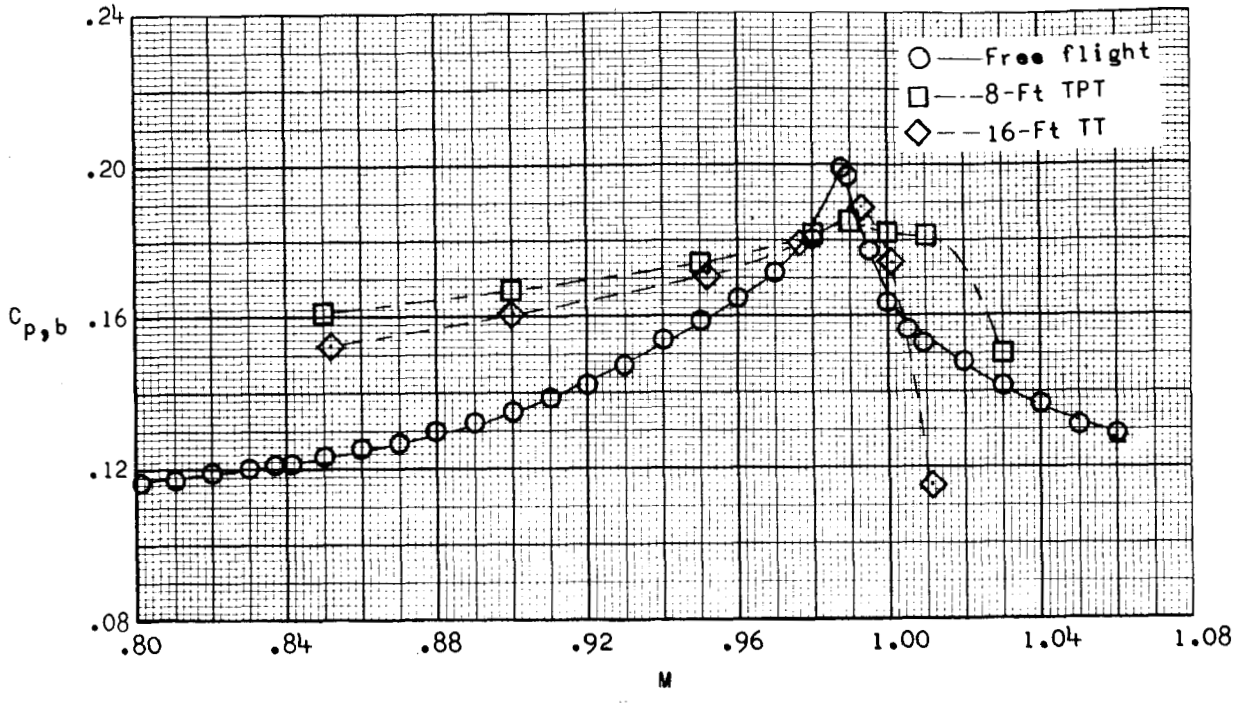

Figure 13.- Variation of base pressure coefficient with Mach number.

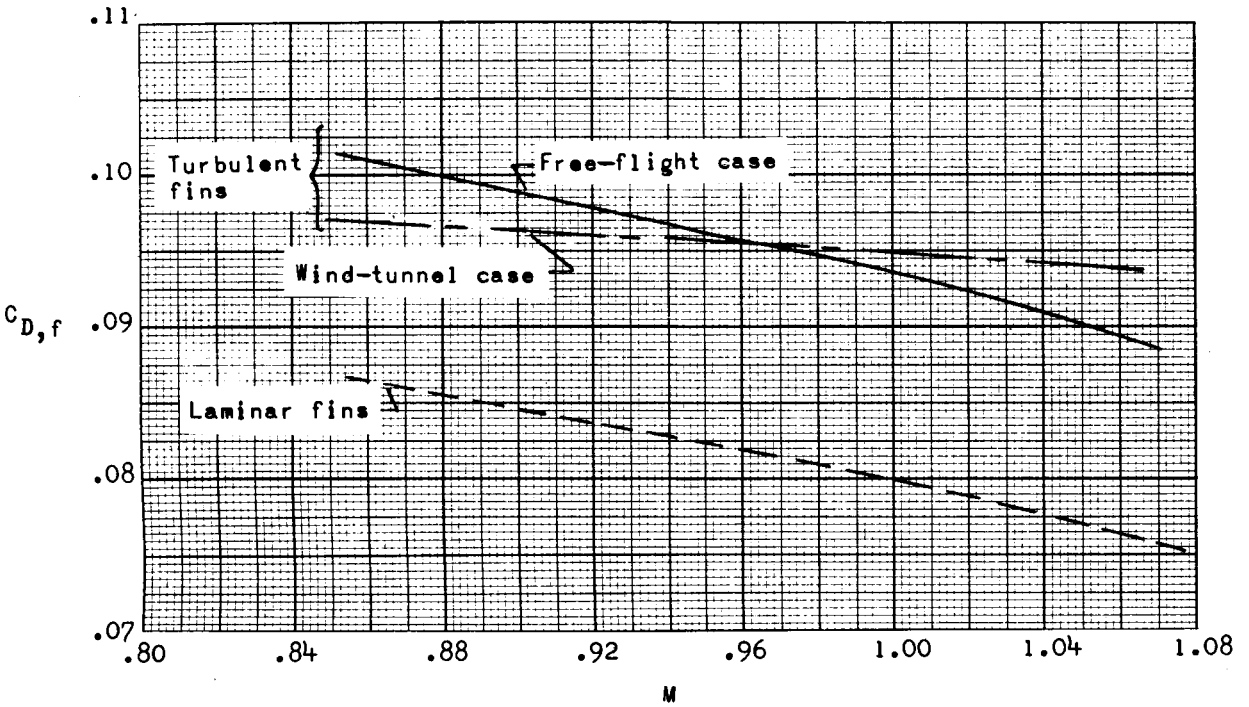

Figure 14.- Variation of theoretical skin-friction drag coefficient with Mach number.

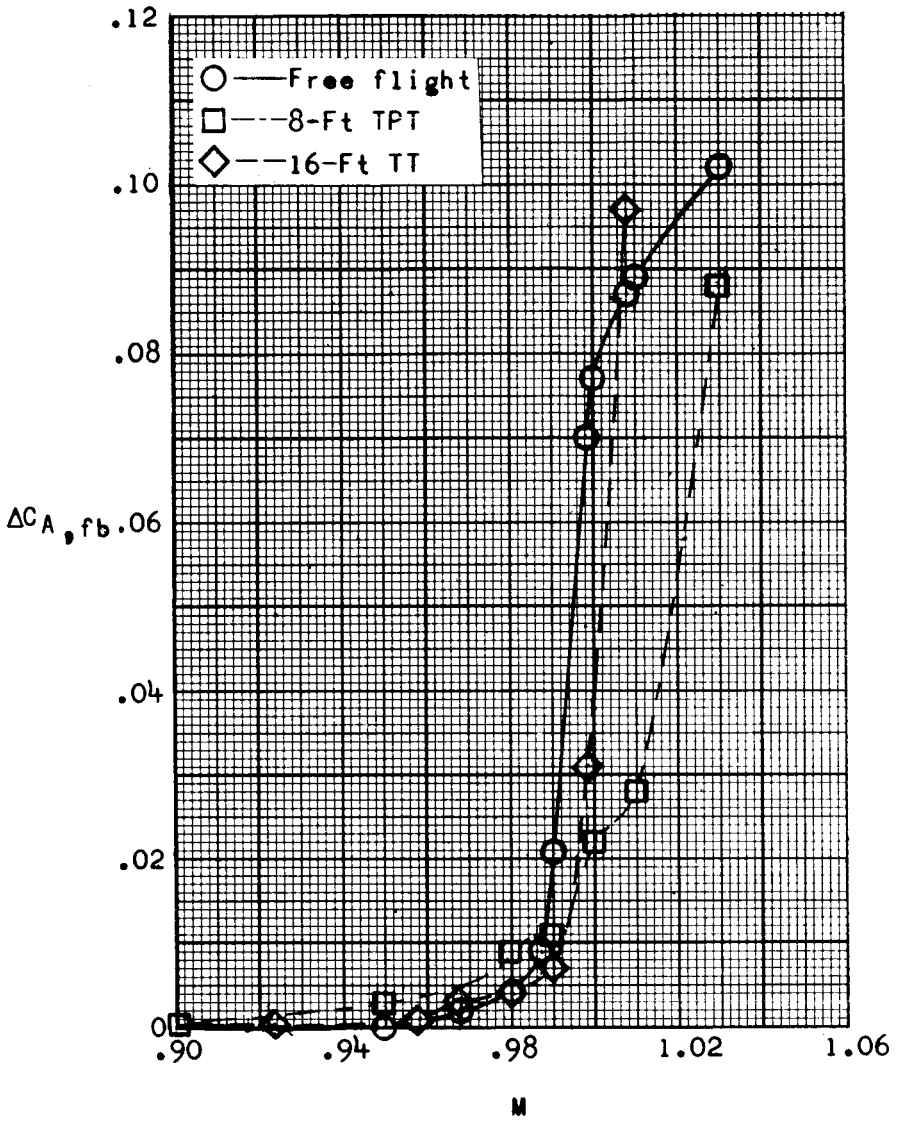

Figure 15.- Comparison of incremental axial-force trends for data from tests in the Langley 8-foot transonic pressure tunnel, the Langley 16-foot transonic tunnel, and in free flight.

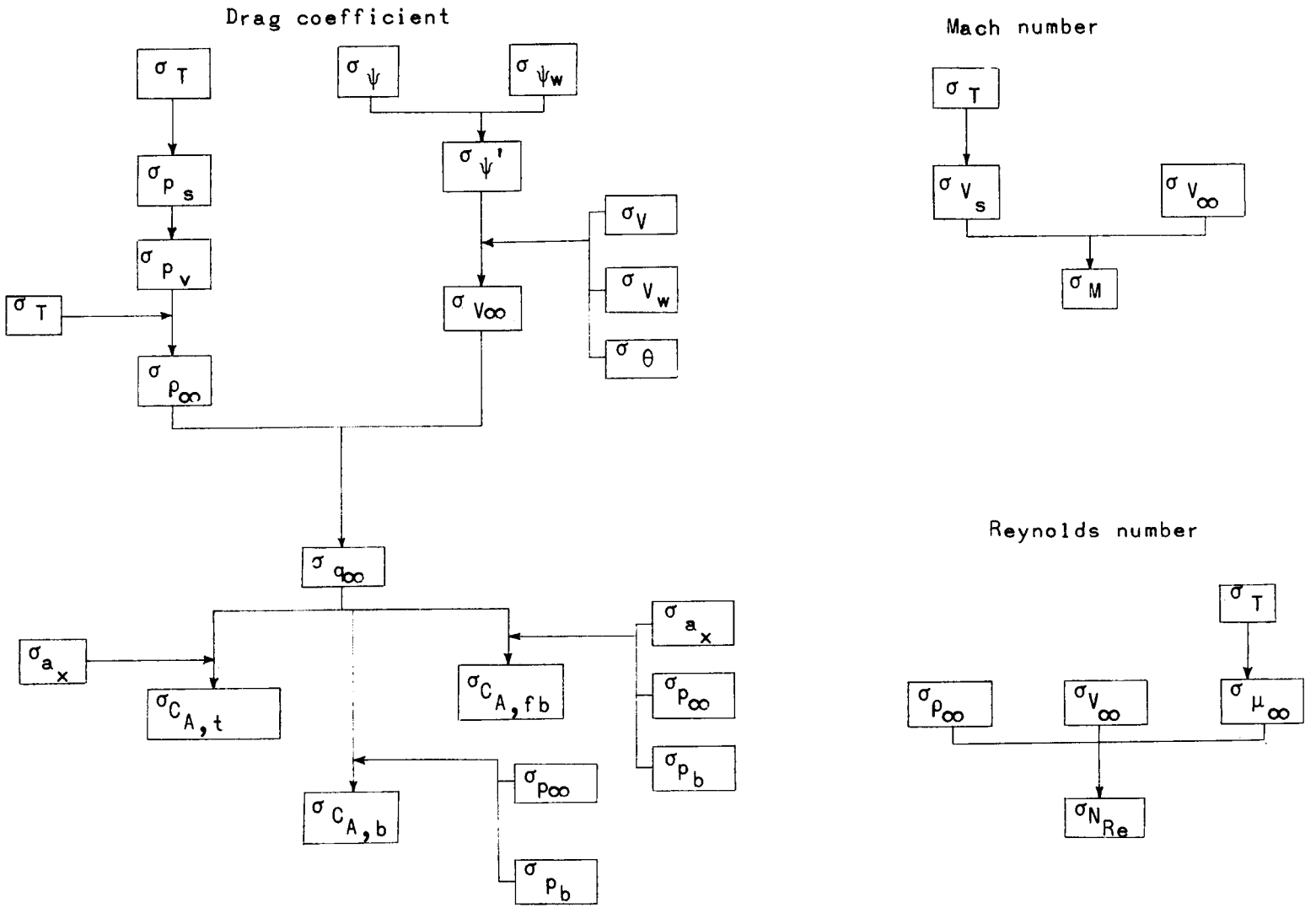

Figure 16.- Flow chart for calculations.

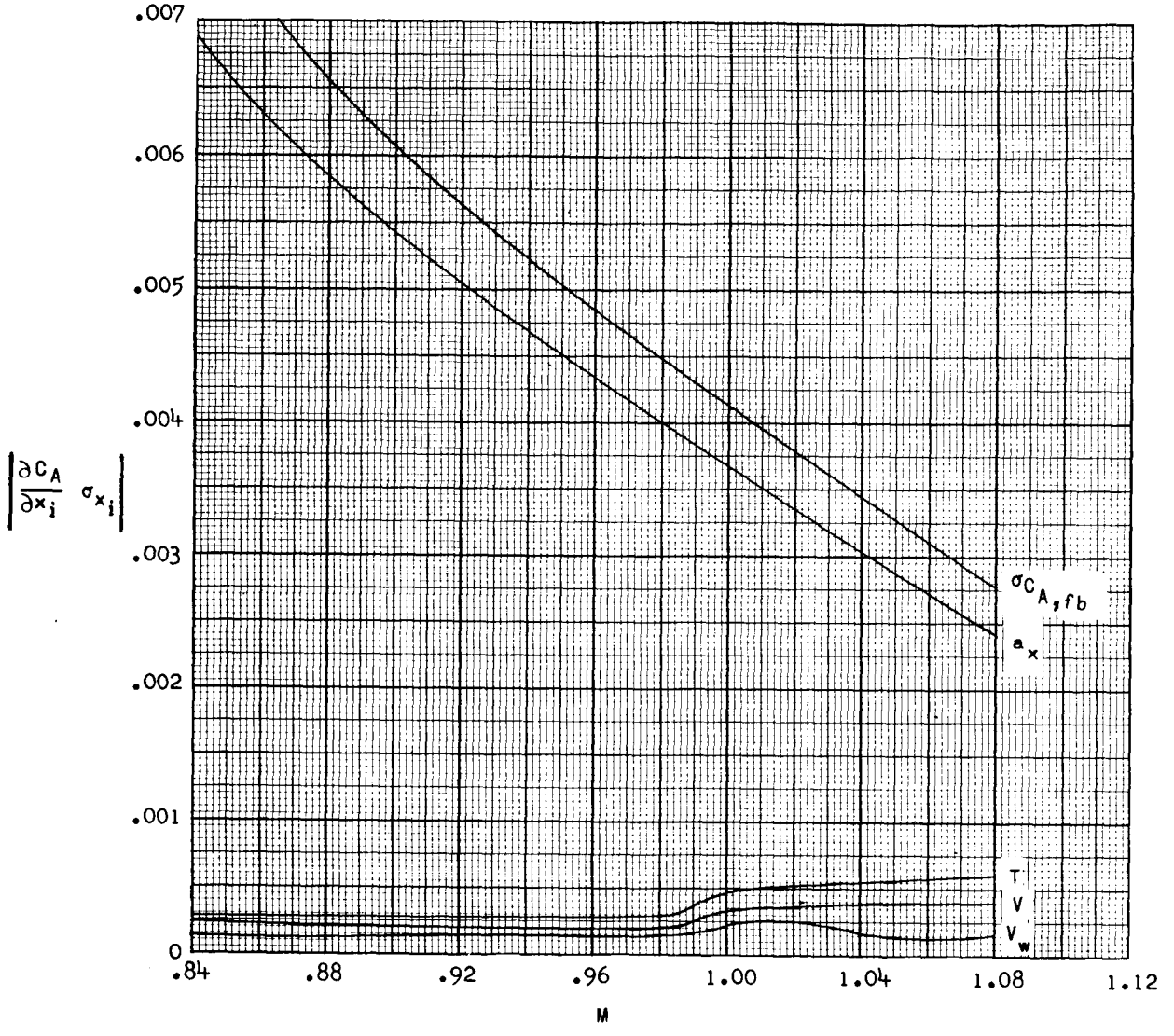

Figure 17.- Variation with Mach number of contribution of variables to σ_{C_A}.

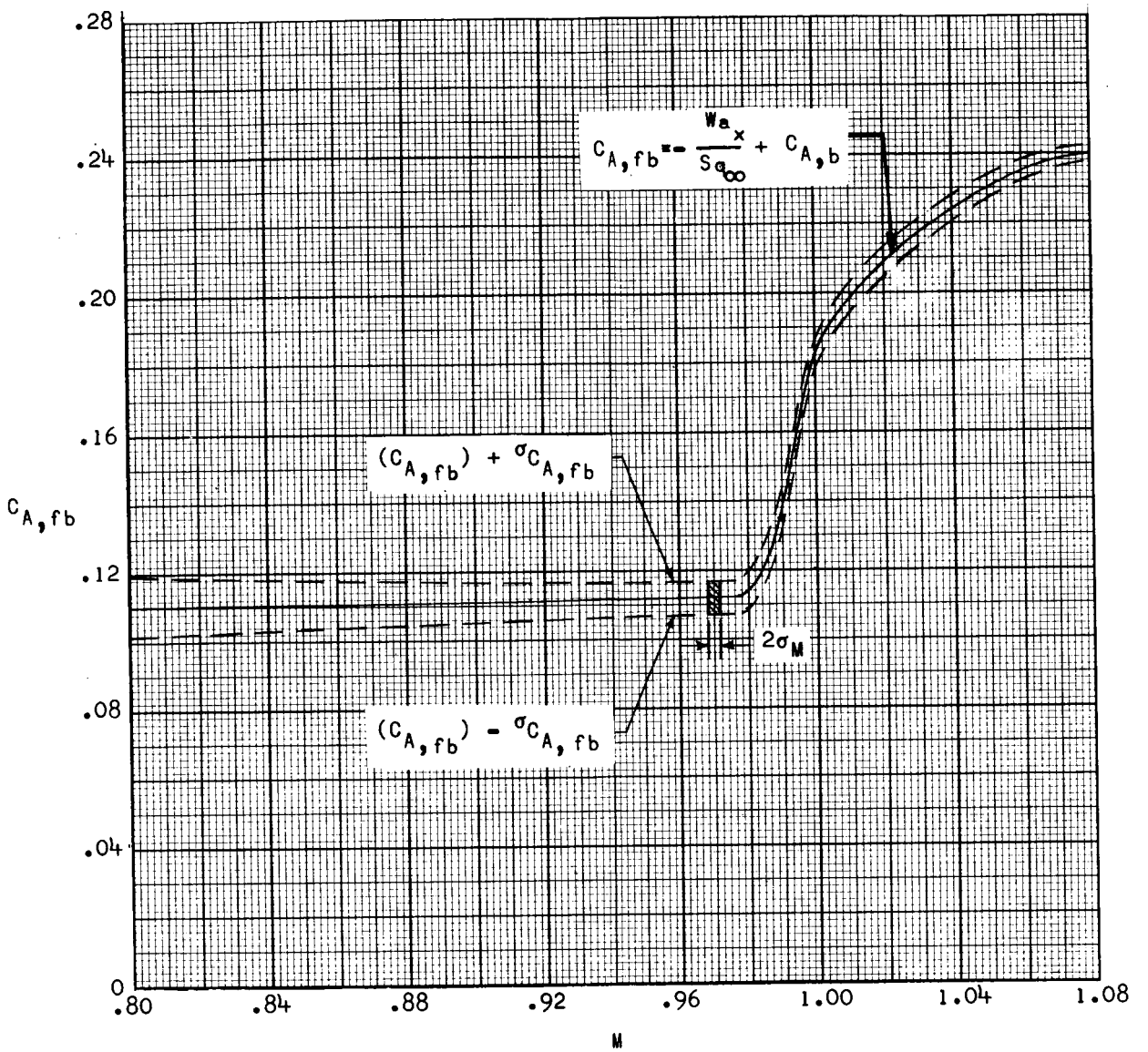

Figure 18.- Variation of drag coefficient and standard deviation with Mach number.